Nanoscale

PAPER

View Article Online
View Journal | View Issue

Cite this: *Nanoscale*, 2025, **17**, 2004

Catalyst-assisted growth of $CsPbBr_3$ perovskite nanowires†

Karam Shreteh, [a] Michael Volokh [a] and Taleb Mokari *[a,b]

Received 31st July 2024,
Accepted 4th December 2024

DOI: 10.1039/d4nr03158j

rsc.li/nanoscale

Halide perovskites (HPs), particularly at the nanoscale, attract attention due to their unique optical properties compared to other semiconductors. They exhibit bright emission, defect tolerance, and a broad tunable band gap. The ability to directly transport charge carriers along the HPs nanowires (NWs) has led to the development of methods for their synthesis. Most of these methods involve some version of an oriented attachment step with various modifications. In this study, we introduce $CsPbBr_3$ nanowires produced *via* the solution–solid–solid (SSS) catalyst-assisted growth mechanism for the first time. We explored the kinetics of this process and examined the connection between the catalyst phase and its reactivity. We show how HP NWs grow with different SSS catalysts (*i.e.*, Ag_2S, Ag_2Se, CuS) and discuss the required conditions for successful synthesis utilizing this mechanism. This method opens up a new avenue for producing HP NWs, which can be used to design and form new types of hybrid nanostructures.

Introduction

Halide perovskites (HPs) have been valued for their unique characteristics in various fields such as photovoltaics,[1,2] optoelectronics,[3,4] and catalysis.[5,6] Lately, the study of quantum-confined colloidal HP nanocrystals has emerged as a significant area of research due to their defect tolerance,[7] wide band gap tunability,[8,9] and bright emission capabilities.[9,10]

As with other semiconductors, the one-dimensional (1D) morphology has been the focus of many studies and applications. New methodologies for synthesizing crystalline HP nanowires (NWs) and nanorods have been developed, driven by the prospect of excellent charge carriers transport within such nanocrystals.[11] For instance, Zhang *et al.* synthesized the first $CsPbBr_3$ perovskite NWs with a diameter of about 10 nm;[12] afterwards, through a stepwise purification process, they managed to reduce the diameter of these NWs to achieve strong quantum confinement at $d \approx 2$ nm.[13] Other homogeneous NWs with a tunable width were also prepared using short chain carboxylic acids and room temperature,[11,14,15] or by harnessing the oriented attachment mechanism, where $CsPbX_3$ (X = halide) cubes assemble to form the desired NW product.[16–18] Due to the cubic nature of these materials, they do not prefer anisotropic growth, as known for wurtzite structures. The previously reported methods are based on the oriented attachment mechanism, where $CsPbX_3$ cubes are attached to form 1D morphology; the synthetic tools that allow this process include low temperature, long time, and changing ligand concentration. However, the catalyst-assisted growth mechanism for growing perovskite nanowires has not yet been reported.

Herein, we describe the synthesis of $CsPbBr_3$ nanowires *via* the solution–solid–solid (SSS) mechanism for the first time. We used semiconductor nanoparticles (Ag_2S, Ag_2Se, Cu_2S) that undergo a phase transition to a superionic phase at the reaction temperature. This reactive phase is typically used as a catalyst for growing metal chalcogenides 1D nanocrystals.[19–21] We succeeded in forming $CsPbBr_3$ perovskite nanowires with μm length in very short synthesis times. Furthermore, we studied the formation kinetics and the effect of the catalyst's type, phase, and composition on the nanowires' growth by real-time monitoring of phase transitions of the catalysts *via in situ* X-ray diffraction (XRD) in solution.

Preparing HPs using the SSS mechanism offers the benefit of catalyst-assisted growth, significantly improving synthesis time and reaction yield. The success of this approach suggests that other catalyst-assisted growth methods, such as solution–liquid–solid (SLS) and vapor–liquid–solid (VLS), could also be employed for HP formation. Notably, these methods are well-suited for large-scale nanowire synthesis, a key factor for advancing nanowire-based device manufacturing.[22,23] Additionally, the flexibility of these catalytic routes holds great potential for

[a]*Department of Chemistry, Ben-Gurion University of the Negev, Beer-Sheva, 8410501, Israel. E-mail: mokari@bgu.ac.il*
[b]*Ilse Katz Institute for Nanoscale Science and Technology, Ben-Gurion University of the Negev, Beer-Sheva, 8410501, Israel*

†Electronic supplementary information (ESI) available: COD (XRD) card numbers, additional (S)TEM images and EDS, UV–vis and PL data. See DOI: https://doi.org/10.1039/d4nr03158j

developing hybrid nanostructures incorporating HPs, thereby broadening the scope of potential applications.[24,25]

Experimental section

Materials

All reactants and solvents were purchased from commercial sources and used as received unless indicated otherwise. Oleylamine (OAm, 98%), dodecanethiol (DDT, 98.5%), oleic acid (OA, 90%), octadecylamine (ODA, 90%), sulfur powder (S, 99.98%), and sodium diethyldithiocarbamate trihydrate ($NadtcEt_2{\cdot}3H_2O$, ≥99.0%; abbreviated in the text as $NadtcEt_2$ for simplicity) were purchased from Sigma-Aldrich. Octadecene (ODE, 90%) and anhydrous toluene (99.8%) were purchased from Alfa Aesar. Anhydrous copper(II) acetate ($CuAc_2$, 97%), cesium carbonate (Cs_2CO_3, 99%), CdO powder (99.999%), and selenium powder (Se, 99.99%) were purchased from Strem. Lead bromide was purchased from Apollo Scientific Limited (PbBr, 99.999%). Silver nitrate ($AgNO_3$, 99.8%) was purchased from Fisher Scientific. The solvents *n*-hexane (C_6H_{14}, 95%), toluene (C_7H_8, 99.7%), 2-propanol (IPA, 99.8%), and ethanol (EtOH, absolute, 99%) were purchased from Bio-Lab Chemicals, Israel.

Synthetic procedures

[$AgdtcEt_2$] preparation. According to previously published procedures,[26] $AgNO_3$ and $NadtcEt_2$ were separately dissolved in deionized water at a 1 : 1 molar ratio. After mixing, stirring, vacuum-filtration, and washing, chloroform was used for recrystallization.

Colloidal syntheses. All the synthetic procedures described hereinafter were conducted using standard air-free Schleck-line techniques (inert N_2 atmosphere), 25 mL three-neck borosilicate round bottom flasks, and PTFE-coated magnetic stirrings bars.

OAm, ODE, and OA were mixed under vacuum at 120 °C overnight before further use.

Ag_2S nanoparticles synthesis. 25 mg of [$AgdtcEt_2$] was mixed with 2 mL OAm and 3 mL DDT under vacuum for 5 min at room temperature; then, the temperature was raised to 200 °C under N_2 atmosphere for 30 min before cooling down to room temperature. 5 mL EtOH was added to the solution for the washing procedure, and after 10 min of centrifugation (4000 rcf), hexane was added to the precipitate until achieving an absorbance of 1.0 at 350 nm. Then, the hexane was evaporated, and 4 mL ODE was added to the precipitate, forming a Ag_2S stock suspension.

Ag_2Se nanoparticles (NPs) synthesis. Ag_2Se NPs were synthesized using a previously published procedure, with some modifications.[27] 0.5 g $AgNO_3$ was mixed in 10 mL ODA at 180 °C for 10 minutes under air; then 120 mg Se was added, and the stirring continued for 10 more min. After cooling to room temperature, the Ag_2Se product was washed several times with EtOH and redispersed in hexane, forming a solution with an absorbance of 1.0 at 473 nm after ×100 dilution. Then, the hexane in 1.5 mL stock solution was evaporated and replaced by 8 mL ODE added to the precipitate, forming a Ag_2Se stock suspension.

Cu_2S nanoparticles synthesis. Cu_2S NPs were synthesized using a previously published procedure, with some modifications.[28] 200 mg $CuAc_2{\cdot}2H_2O$ was mixed in 10 mL DDT under N_2 atmosphere, then the temperature was raised to 220 °C and kept for 30 minutes before cooling to room temperature and washed several times with EtOH. Toluene was added until reaching an absorbance value of 1.0 at 421 nm. The toluene in the stock solution (*ca.* 3 mL) was evaporated, and 8 mL ODE was added to the precipitate, forming a Cu_2S stock suspension.

CdS nanoparticles synthesis. CdO powder (16 mg) was mixed with 1.5 mL OA and 4 mL ODE under vacuum for 20 min at room temperature; then, the temperature was raised to 120 °C under N_2 atmosphere for 30 min. Then, at 265 °C, 0.87 mL S-ODE solution (10 mg S powder mixed in 3 mL ODE for 2 h at 60 °C) was injected; after 10 minutes incubation at 250 °C the solution cooled down to room temperature and underwent several cycles of washing (using IPA) and redispersion (in 4 mL toluene), forming the Cu_2S stock suspension.

Cs-OA solution preparation. 19.5 mg Cs_2CO_3 and 0.1 mL OA were mixed in 10 mL ODE, held under vacuum for 30 minutes at 120 °C, and then incubated for 15 minutes at 150 °C under an N_2 atmosphere, forming a clear solution. Immediately before use, the solution is heated to 100 °C to allow injection of a liquid clear solution.

$PbBr_2$ solution preparation. 69 mg $PbBr_2$ was mixed with 0.5 mL OAm and 0.5 mL OA in 5 mL anhydrous toluene under N_2 atmosphere at 100 °C until dissolving the $PbBr_2$ salt (~1.5 h). This solution is diluted ×10 for use in the washing process.

$CsPbBr_3$ NWs synthesis. $PbBr_2$ and cesium oleate solutions were prepared separately. 20 mg $PbBr_2$ was mixed in 5 mL ODE and 1 mL OA at 120 °C under vacuum for one hour as a purification step. Then, after changing the atmosphere to N_2, 0.5 mL dry OAm was injected before raising the temperature to 190 °C; during the heating process, the $PbBr_2$ salt dissolved, changing the reaction solution's color to a clear yellow; at this point, 0.2 mL Ag_2S/Ag_2Se solution was injected followed by hot (~100 °C) 0.35 mL Cs-OA solution injection. After 5 minutes, the synthesis was quenched with a water bath, and the solution was centrifuged (8000 rcf) for 5 minutes. 5 mL anhydrous toluene was added to the precipitate, followed by 0.1 mL dry OAm and 0.5 mL $PbBr_2$ solution, shaken for 2 minutes and centrifuged (4000 rcf) for 6 minutes. The described wash was repeated twice more but without OAm. The resulting precipitate at the end of the washing procedure was finally dispersed in anhydrous toluene for further characterization.

For the Cu_2S-catalyzed $CsPbBr_3$ NWs synthesis, we use a similar procedure, but with 220 °C reaction temperature and 0.2 mL Cu_2S solution that was injected after the temperature raises back to the 220 °C setpoint after the OAm injection.

***In situ* XRD experiments.** The experimental setup follows the procedure published by our group.[29] The reaction mixture was

prepared by taking 3 mL of Ag_2S in hexane suspension (absorbance of 1.0 at 421 nm), evaporation of the hexane, followed by addition of 150 μL ODE and mixing for 60 min under N_2 atmosphere. The resulting slurry was placed inside a commercial HTK1200 0.8 mm deep sample carrier. The sample carrier was then placed on the sample holder, which was inserted and fixed inside the environmental heating chamber, which was then purged and filled with He (g) for 30 min. A pre-planned non-ambient program in the Data Collector software (Malvern PANalytical) regulated the temperature of the oven and the timing of the XRD scans. The temperature in the oven chamber was elevated at a heat ramp of 30 °C min^{-1} for all the measurements performed in a scan window (2θ values) of 39–48° and the scan duration of each pattern was set to 9 min. At each temperature setpoint, the sample remained for 18 minutes, including the measurement and 9 minutes of incubation before.

Characterization

Instruments and techniques. Transmission electron microscopy (TEM), high-resolution TEM (HRTEM), and scanning TEM (STEM) imaging were conducted using a JEOL JEM-2100F analytical TEM operated at 200 keV and equipped with a GATAN 894 US1000 camera.

Energy-dispersive X-ray spectroscopy (EDS) analysis was performed using a JEOL JEM-2100F TEM operated at 200 kV and equipped with an Oxford Instruments X-Max 65T SDD detector. The probe size during the analysis was set to 1 nm. AZtec software (v. 3.3) was used for the EDS data analysis.

High resolution STEM (HRSTEM) imaging was conducted using Spectra 200 (Thermo Fisher Scientific) with a Cs-corrected probe (S-CORR) scanning transmission electron microscope (S/TEM) operated at 200 kV. The images were recorded in STEM mode with a high-angle annular dark field (HAADF) detector.

Ex situ XRD measurements were conducted using Panalytical Empyrean III (Malvern Panalytical) multi-purpose diffractometer equipped with a Cu X-ray source (Cu K_α, λ = 1.5406 Å), operated at 45 kV and 40 mA. The instrument was equipped with the iCore–dCore automated XRD optics combination, a PixCEL 3D detector in 1D line-detector mode. Measurements were recorded of dry samples after drop-casting on (100) single-side polished Si substrates.

In situ XRD measurements were conducted using Panalytical Empyrean (Malvern Panalytical) diffractometer equipped with an X'Celerator detector using Cu K_α radiation (λ = 1.5406 Å), operated at 45 kV and 40 mA recording in Anton Paar's HTK 1200N high-temperature oven chamber with an aluminum oxide sample holder as a sample stage for continuous XRD monitoring at different temperatures. The chamber was filled with He(g) to maintain an inert atmosphere.

UV–vis absorption was measured using an Edinburgh Instruments DS5 dual beam spectrophotometer with tungsten halogen and deuterium light sources and quartz cuvettes with an optical path of 10 mm.

Photoluminescence (PL) spectra were collected using Varian Cary Eclipse fluorimeter, exciting the samples at λ_{exc} = 410 nm.

Results and discussion

The synthetic process commences by mixing $PbBr_2$ powder and oleic acid in ODE. Following a purification step under vacuum at 120 °C (as detailed in Experimental section), oleylamine is added to the mixture. As the temperature rises to 190 °C, the mixture changes color to clear yellow due to the complexation of the $PbBr_2$. Subsequently, Ag_2S NPs (Fig. S1†) dispersion (see full details in the Experimental section) is injected, followed by the injection of a cesium oleate (Cs-OA) solution. After 5 minutes, thin (d ~5 ± 1 nm, Fig. S2†) NWs with both spherical and cubic tips form, as depicted in the TEM image in Fig. 1a. EDS mapping (Fig. 1b and Fig. S2†) reveals that the spherical tips consist of silver (light blue) and sulfur (green), corresponding to the Ag_2S NPs introduced during synthesis. Meanwhile, the NWs comprise cesium (yellow), lead (purple), and bromine (red).

The UV–vis absorbance spectrum in Fig. 1c exhibits a peak at 494 nm, characteristic of perovskite $CsPbBr_3$ NWs, with a corresponding single PL emission peak centered about 511 nm.

Interestingly, although there are Ag_2S NPs on the tip of each NW, their absorbance is not evident in the UV–vis spectrum. This discrepancy can be attributed to the negligible amount of Ag_2S relative to the long $CsPbBr_3$ NWs, which can reach lengths of 1–2 μm, as observed in the high-angle annular dark-field scanning transmission electron microscopy

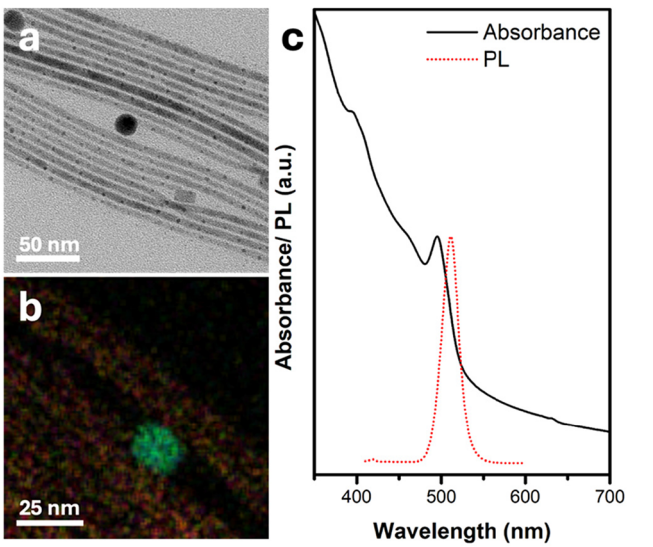

Fig. 1 Characterization of Ag_2S-catalyzed $CsPbBr_3$ NWs. (a) TEM image, (b) elemental EDS map—silver in light blue, sulfur in green, cesium in yellow, lead in purple, and bromine in red, and (c) UV–vis absorbance and photoluminescence (PL) spectra in black dotted red lines, respectively (λ_{exc} = 410 nm). The dark field STEM image and individual elemental maps corresponding to panel (b) appear in Fig. S3.†

(HAADF-STEM) image in Fig. S4.† nanowires are shown in Fig. 2. The high-resolution TEM (HRTEM) image in Fig. 2a shows the NW's tip with a darker contrast, exhibiting the (122) and (102) crystallographic planes of monoclinic Ag_2S. Further characterizations of the crystallographic structure of the nanowires are shown in Fig. 2. The NW, close to the interface with the Ag_2S NP tip, shows a brighter contrast and displays the (101) planes of the cubic perovskite $CsPbBr_3$ phase (d_{101} = 4.12 Å). The X-ray diffraction (XRD) pattern (Fig. 2b) corroborates the cubic perovskite $CsPbBr_3$ phase formation. Notably, the diffractions attributed to (100) and (200) exhibit higher relative intensity compared to the literature bulk diffraction card (red sticks at the bottom of Fig. 2b).

This phenomenon is explained by examining the HRSTEM image in Fig. 2c, which depicts $CsPbBr_3$ NWs with the ⟨100⟩ growth direction; this orientation of the 1D structure leads to an enhanced relative intensity of the (100) and (200) planes compared to bulk 3D cubic phase.

We attribute the observed growth mechanisms to the SSS mechanism.[19] Ag_2S NPs that serve as catalysts transform from the monoclinic phase at room temperature to the superionic cubic phase at high temperatures (bulk phase transition temperature, $T_{tr,\ bulk}$ = 179 °C).[30] Typically, this mechanism catalyzes the formation of one-dimensional metal chalcogenide NPs.[31–34] Here, we demonstrate the formation of $CsPbBr_3$ perovskite NWs for the first time using an SSS catalyst-assisted growth mechanism. A control experiment was conducted to validate this by carrying out the synthesis under the same conditions except for adding the Ag_2S NPs. The TEM image of the outcome product of this experiment (Fig. S5†) shows the formation of only typical cubes and 2D sheets of cubic phase $CsPbBr_3$ with no nanowires. To better understand the effect of the temperature on the nanowires' formation, we synthesized $CsPbBr_3$ NWs at 170 °C (lower than the $T_{tr,\ bulk}$ of Ag_2S). $CsPbBr_3$ NWs still formed even at this lower temperature (Fig. 3a). This observation indicates that the catalyst is still reactive, which can be attributed to the size effect of the Ag_2S NPs, where the transition temperature is expected to be lower than that of the bulk one.[19,35]

For further investigation and study of the catalyst transition temperature effect, $CsPbBr_3$ nanowires were synthesized at two temperatures (Fig. 3b and c): at 140 °C, we observed a mixture of rectangular nanoparticles and a minor nanowire product, while at 120 °C, only rectangular $CsPbBr_3$ NPs and unreacted Ag_2S nanoparticles were present. These results show that at 140 °C a partial phase transformation occurs; in contrast, at 120 °C Ag_2S remains inactive since it is below the transformation temperature.

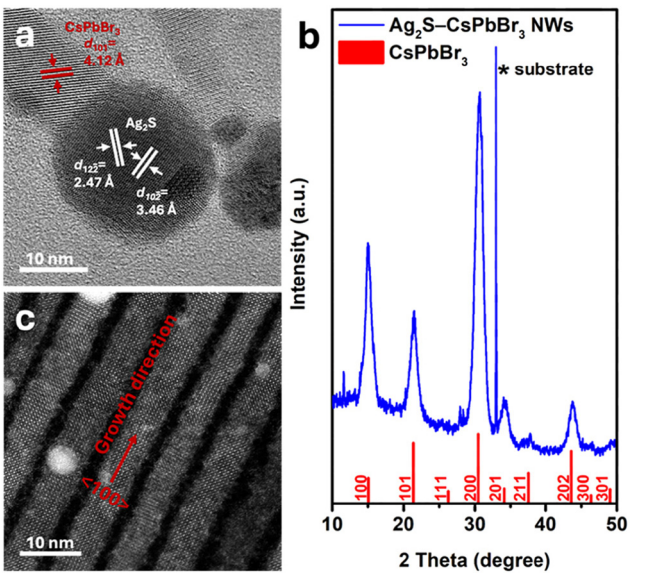

Fig. 2 Crystallographic characterization of Ag_2S-catalyzed $CsPbBr_3$ NWs. (a) HRTEM image, (b) XRD pattern, and (c) HRSTEM image. The asterisk (*) in the XRD pattern analysis denotes a diffraction from the single-sided polished Si substrate.

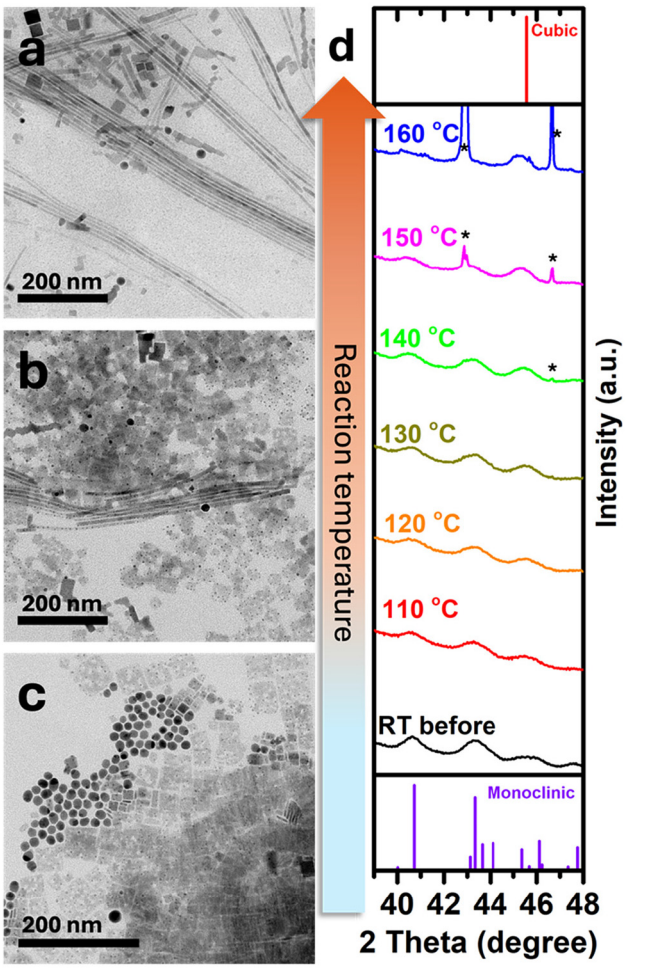

Fig. 3 Ag_2S activity as an SSS catalyst as a function of temperature. TEM image of Ag_2S-catalyzed $CsPbBr_3$ NWs (a) at 170 °C, (b) at 140 °C, and (c) at 120 °C. (d) *In situ* XRD patterns of Ag_2S NPs in ODE as a function of temperature (in the 110–160 °C range); the asterisks (*) denote diffractions from the corundum crucible in which the measurement was monitored.

To investigate this transition in the reported system, we performed *in situ* XRD measurements[29] of Ag_2S NPs in ODE (similar conditions to the original synthesis). As shown in Fig. 3d at room temperature (black pattern; bottom), Ag_2S NPs exhibit a monoclinic phase with dominant diffraction signals at 40.7° and 43.3° and a small peak at 45.5°. At 160 °C (blue pattern; top), a complete transformation into the superionic cubic phase occurs, with a single diffraction peak about 2θ = 45.5° attributed to the (211) plane (this position is close to the (112) plane of the monoclinic phase). The phase transition is evident from the changing ratio between the diffraction at 43.3° and 45.5°. At 130 °C (olive green pattern) and above, the experimental diffraction peak at *ca.* 45.5° becomes similar in intensity to the peak at 43.3°, indicating the partial transformation of some Ag_2S NPs into the cubic phase. The overlap between the two phases increases the experimental intensity at 45.5° until it becomes the dominant peak after complete transformation at 160 °C.

Together with the TEM images (Fig. 3b and c) it confirms that $CsPbBr_3$ NWs formation is temperature-dependent since the temperature determines Ag_2S's phase, thus its catalytic activity, supporting the $CsPbBr_3$ NWs growth mechanism being SSS.

One may expect that NWs synthesized *via* an SSS mechanism, like all catalyst-assisted growth nanowires, would have a catalyst decorating each tip. However, some NWs lack this feature (notably in the TEM images shown in Fig. 3). Yang and colleagues attributed this to the fragile nature of these materials and extensive purification, which can damage and break the NWs in their work on $CsPbBr_3$ NWs preparation.[13]

We also noticed that the interface between the Ag_2S catalyst and the $CsPbBr_3$ NW is the weakest point, as shown in Fig. S6.† During image scanning, the HRSTEM image shows a separation between the two domains at the interface. This suggests that NWs without tips are either NW fragments or NWs that have lost their tip before imaging.

A kinetic study confirmed that each NW has a tip (a requirement for an SSS mechanism). In each separate synthesis, the reaction was quenched using a water bath at different times. The first synthesis was quenched immediately after the Cs-OA injection. As demonstrated in Fig. 4a, even after this brief reaction, $CsPbBr_3$ NWs form, measuring around 100 ± 20 nm (Fig. S2†) in length.

This length allows us to observe both ends of the NWs: each NW has the spherical Ag_2S catalyst on the tip (dark contrast in the TEM image); some NWs have a cube at the other end, which will be discussed later. The short length of these NWs (Fig. 4a) can be explained by the relationship between the reaction temperature and the catalytic activity that we demonstrated in Fig. 3. The quenching process from 190 °C to the inactive 130 °C temperature takes 3–4 seconds, meaning even when reaction quenching is attempted, the catalyst remains active for about 3–4 s, which is sufficient for a 100 nm growth.

In Fig. 4b, where the synthesis was quenched 5 seconds later, the NWs grew to lengths of about 310 ± 90 nm (Fig. S2†). Most of them have a spherical tip supporting the SSS mechanism and a cube on the other side. Fig. S7† shows an HRSTEM image of five distinct NW tips from the same sample presented in Fig. 4b; two of them have the spherical Ag_2S catalyst, and the others exhibit a cube-shaped tip that matches the same $CsPbBr_3$ perovskite phase as the NW itself. The discussed $CsPbBr_3$ cube is located opposite to the growth direction, leading us to believe that it forms at the beginning of the reaction. After the fast injection of Cs-OA, we propose that two processes occur concurrently: NW growth *via* an SSS mechanism and the typical $CsPbBr_3$ nucleation and growth ('regular' growth mechanism). Most self-nucleated $CsPbBr_3$ are washed out during the washing process, but the newly formed $CsPbBr_3$ NW tip (*via* SSS) can also serve as a nucleus for a cube that would form on the older side of each NW by the end of the reaction. Therefore, as expected, the $CsPbBr_3$ cubes also appear in the longer NWs (longer reaction times shown in Fig. 4c and d) and sometimes even on some NW fragments.

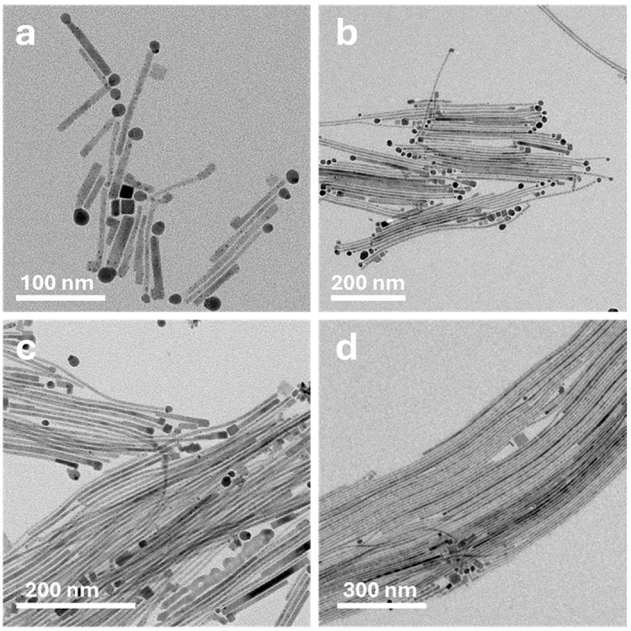

Fig. 4 TEM images of Ag_2S-catalyzed $CsPbBr_3$ NWs reaction stages at different quenching times: (a) immediate quenching, (b) 5 s, (c) 1 min, and (d) 5 min.

Rogach and co-workers noted that the perovskite $CsPbBr_3$ crystallization process is very fast and takes 3–10 seconds to form cube-shaped NPs.[36] This can explain why some of the short NWs in Fig. 4a do not have cubes on the tips.

During the described quenching process, the 3–10 seconds timeframe—which is required for the cube formation—is sufficient for cooling down the reaction medium to a temperature that prevents some of the cubes from crystallizing. However, these images explain the difference between the tips and show the temporal control over the NW length. Most importantly, they illustrate how fast this catalytic process occurs compared to other synthetic methods yielding $CsPbBr_3$ NWs.

Thus far, we have demonstrated that Ag_2S NPs can act as catalysts for forming $CsPbBr_3$ NWs. However, this is not unique to Ag_2S, as other materials with a superionic phase can

also catalyze SSS growth. We first replaced Ag_2S with Ag_2Se, another known SSS catalyst. As seen in the TEM image (Fig. 5a), thin NWs with both spherical and cubical tips were formed, similar to those catalyzed by Ag_2S. EDS mapping and spectra (Fig. S8 and S9†) confirm that the spherical Ag_2Se catalyst is linked to the $CsPbBr_3$ NW. Furthermore, the HRTEM image (Fig. 5b) shows that the darker contrast sphere corresponds to the orthorhombic Ag_2Se phase, while the NW linked to these Ag_2Se NPs is in the cubic perovskite $CsPbBr_3$ phase. The UV–vis absorbance spectrum of the entire sample also shows the characteristic absorbance of $CsPbBr_3$ perovskites with a local absorbance maximum at 493 nm and a PL emission at 516 nm (Fig. S10†).

Additionally, we have used Cu_2S as the SSS catalyst. This experiment aimed to demonstrate the synthesis' generality and show that the growth is not solely dependent on the presence of silver in the system. For the synthesis with Cu_2S, we increased the reaction temperature to 220 °C to form the NWs (Fig. 5c), which is inconsistent with the simple relationship between the catalytic activity and temperature, as observed and described for the Ag_2S system. The active superionic phase transition of Cu_2S is $T_{tr,\ bulk}$ = 105 °C;[37] however, even at 190 °C, where the Cu_2S is indeed in the active superionic phase, no NWs formed, suggesting that the phase transition is not the only factor affecting the reactivity of SSS catalysts.

The synthesis of the HP NWs using Cu_2S catalyst has a lower yield compared to other two catalyst systems, possibly due to a combination of two reasons: (i) the relatively low reactivity of Cu_2S, as observed in other works,[19] and (ii) at higher temperatures, the self-nucleation process becomes more dominant, consuming the $CsPbBr_3$ at the expense of the SSS process, which leads to lower NW yield. However, $CsPbBr_3$ NWs form in the presence of a Cu_2S catalyst, as shown in Fig. 5d; the darker contrast monoclinic Cu_2S phase tip connects to a $CsPbBr_3$ cubic perovskite phase NW, as expected from an SSS growth. The quantitative EDS spectra in Fig. S11† corroborate this analysis. To further prove the necessity of the superionic phase, we conducted a control experiment and replaced the catalyst with cubic CdS NPs (Fig. S12a†), keeping all other experimental conditions the same. As shown in Fig. S12b,† no NWs formed. This suggests that a requirement for a cubic phase or a chalcogenide material from a NP is not sufficient to allow $CsPbBr_3$ NWs growth; an active superionic phase (such as Ag_2S, Ag_2Se, or Cu_2S) is required for a successful catalyst-assisted SSS NW growth.

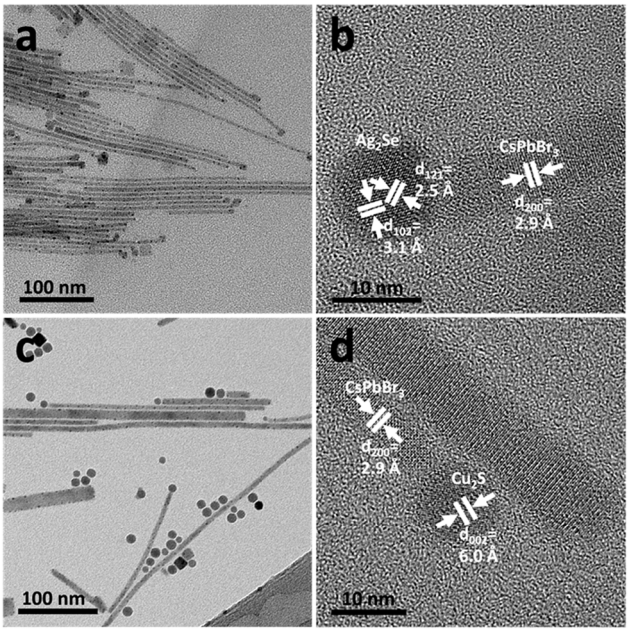

Fig. 5 $CsPbBr_3$ NWs synthesized with SSS catalysts. (a) TEM and (b) HRTEM images of Ag_2Se-catalyzed NWs. (c) TEM and (d) HRTEM images of Cu_2S-catalyzed NWs.

Conclusion

In conclusion, we have devised a novel approach to synthesize $CsPbBr_3$ perovskite NWs using a catalyst-assisted growth mechanism. For the first time, we have synthesized $CsPbBr_3$ perovskite NWs using superionic Ag_2S NPs as a growth catalyst —a previously employed technique for 1D metal chalcogenides materials preparation. We have demonstrated the growth kinetics, highlighting the catalytic process' speed. We have also illustrated how the phase transition of the catalyst at varying temperatures influences the final product and how versatile this method is by employing other known superionic SSS catalysts (specifically, Ag_2Se and Cu_2S). This technique paves a new way for forming HP NWs, demonstrating that these materials can be produced using catalyst-assisted growth methods such as solution–liquid–solid and vapor–liquid–solid.[38,39] We envision that such catalyst-assisted growth methods would be beneficial for forming hybrid nanostructures that incorporate these HPs,[24,34] or for fabricating arrays that can be integrated into devices.[40]

Data availability

The data supporting this article have been included as part of the ESI. COD (XRD) card numbers, additional (S)TEM images and EDS, UV–vis and PL data.

Conflicts of interest

There are no conflicts to declare.

Acknowledgements

This work was supported by the Israeli Science Foundation (ISF, grant no. 1507/22). The authors thank Dr Vladimir Ezersky for helpful discussions and for high-resolution and analytical TEM. K. S. thanks the chemo-tech fellowship from the Kreitman School of Advanced Graduate Studies, Ben-

Gurion University of the Negev, and the Council for Higher Education fellowship for outstanding doctoral students from the Arab community.

References

1 A. Kojima, K. Teshima, Y. Shirai and T. Miyasaka, *J. Am. Chem. Soc.*, 2009, **131**, 6050–6051.
2 P. Li, X. Liu, Y. Zhang, C. Liang, G. Chen, F. Li, M. Su, G. Xing, X. Tao and Y. Song, *Angew. Chem., Int. Ed.*, 2020, **59**, 6909–6914.
3 J. Xue, Z. Zhu, X. Xu, Y. Gu, S. Wang, L. Xu, Y. Zou, J. Song, H. Zeng and Q. Chen, *Nano Lett.*, 2018, **18**, 7628–7634.
4 P. Docampo and T. Bein, *Acc. Chem. Res.*, 2016, **49**, 339–346.
5 L. Wu, Y. Mu, X. Guo, W. Zhang, Z. Zhang, M. Zhang and T. Lu, *Angew. Chem., Int. Ed.*, 2019, **58**, 9491–9495.
6 P. Chen, W. J. Ong, Z. Shi, X. Zhao and N. Li, *Adv. Funct. Mater.*, 2020, **30**, 1909667.
7 M. V. Kovalenko, L. Protesescu and M. I. Bodnarchuk, *Science*, 2017, **358**(6364), 745–750.
8 Y. Tong, E. Bladt, M. F. Aygüler, A. Manzi, K. Z. Milowska, V. A. Hintermayr, P. Docampo, S. Bals, A. S. Urban, L. Polavarapu and J. Feldmann, *Angew. Chem., Int. Ed.*, 2016, **55**, 13887–13892.
9 L. Protesescu, S. Yakunin, M. I. Bodnarchuk, F. Krieg, R. Caputo, C. H. Hendon, R. X. Yang, A. Walsh and M. V. Kovalenko, *Nano Lett.*, 2015, **15**, 3692–3696.
10 H. Utzat, W. Sun, A. E. K. Kaplan, F. Krieg, M. Ginterseder, B. Spokoyny, N. D. Klein, K. E. Shulenberger, C. F. Perkinson, M. V. Kovalenko and M. G. Bawendi, *Science*, 2019, **363**, 1068–1072.
11 Y. Wang, X. Liu, Q. He, G. Chen, D. Xu, X. Chen, W. Zhao, J. Bao, X. Xu, J. Liu and X. Wang, *Adv. Funct. Mater.*, 2021, **31**, 202011251.
12 D. Zhang, S. W. Eaton, Y. Yu, L. Dou and P. Yang, *J. Am. Chem. Soc.*, 2015, **137**, 9230–9233.
13 D. Zhang, Y. Yu, Y. Bekenstein, A. B. Wong, A. P. Alivisatos and P. Yang, *J. Am. Chem. Soc.*, 2016, **138**, 13155–13158.
14 M. Imran, F. Di Stasio, Z. Dang, C. Canale, A. H. Khan, J. Shamsi, R. Brescia, M. Prato and L. Manna, *Chem. Mater.*, 2016, **28**, 6450–6454.
15 Y. Liu, M. Guo, S. Dong, X. Jiao, T. Wang and D. Chen, *J. Mater. Chem. C*, 2018, **6**, 7797–7802.
16 Y. Tong, B. J. Bohn, E. Bladt, K. Wang, P. Müller-Buschbaum, S. Bals, A. S. Urban, L. Polavarapu and J. Feldmann, *Angew. Chem., Int. Ed.*, 2017, **56**, 13887–13892.
17 J. Liu, K. Song, Y. Shin, X. Liu, J. Chen, K. X. Yao, J. Pan, C. Yang, J. Yin, L.-J. Xu, H. Yang, A. M. El-Zohry, B. Xin, S. Mitra, M. N. Hedhili, I. S. Roqan, O. F. Mohammed, Y. Han and O. M. Bakr, *Chem. Mater.*, 2019, **31**, 6642–6649.
18 L. He, S. Pan, Z. Lin and J. Peng, *ACS Appl. Nano Mater.*, 2019, **2**, 7910–7915.
19 J. Wang, K. Chen, M. Gong, B. Xu and Q. Yang, *Nano Lett.*, 2013, **13**, 3996–4000.
20 Q. Li, C. Zou, L. Zhai, L. Zhang, Y. Yang, X. Chen and S. Huang, *CrystEngComm*, 2013, **15**, 1806.
21 Y. Li, Z.-C. Shao, C. Zhang and S.-H. Yu, *J. Phys. Chem. Lett.*, 2021, **12**, 10695–10705.
22 F. Wang, A. Dong and W. E. Buhro, *Chem. Rev.*, 2016, **116**, 10888–10933.
23 Y. Sun, T. Dong, L. Yu, J. Xu and K. Chen, *Adv. Mater.*, 2019, **32**, 1903945.
24 K. Shreteh, M. Volokh, V. Ezersky and T. Mokari, *Chem. Mater.*, 2021, **33**, 4701–4708.
25 N. Afik, K. Shreteh, H. Fridman, M. Volokh, V. Ezersky and T. Mokari, *Chem. Mater.*, 2021, **33**, 9326–9333.
26 K. Shreteh, S. Murugesan, I. Alkrenawi, N. Afik, M. Volokh and T. Mokari, *Inorg. Chem.*, 2024, **63**, 431–440.
27 D. Wang, T. Xie, Q. Peng and Y. Li, *J. Am. Chem. Soc.*, 2008, **130**, 4016–4022.
28 Z. Zhuang, X. Lu, Q. Peng and Y. Li, *Chem. – Eur. J.*, 2011, **17**, 10445–10452.
29 H. Fridman, M. Volokh and T. Mokari, *Nanoscale*, 2021, **13**, 19076–19084.
30 S. Hoshino, *Solid State Ionics*, 1991, **48**, 179–201.
31 F. Wang and W. E. Buhro, *ACS Nano*, 2017, **11**, 12526–12535.
32 T. Zhuang, P. Yu, F. Fan, L. Wu, X. Liu and S. Yu, *Small*, 2014, **10**, 1394–1402.
33 W. Han, L. Yi, N. Zhao, A. Tang, M. Gao and Z. Tang, *J. Am. Chem. Soc.*, 2008, **130**, 13152–13161.
34 Y. Li, C. Zhang, T.-T. Zhuang, Y. Lin, J. Tian, X.-Y. Qi, X. Li, R. Wang, L. Wu, G.-Q. Liu, T. Ma, Z. He, H.-B. Sun, F. Fan, H. Zhu and S.-H. Yu, *J. Am. Chem. Soc.*, 2021, **143**, 7013–7020.
35 J. Liu, L. Chen, H. Yang, Z. Zhang and Y. Wang, *Prog. Nat. Sci.: Mater. Int.*, 2019, **29**, 397–401.
36 K. Vighnesh, S. Wang, H. Liu and A. L. Rogach, *ACS Nano*, 2022, **16**, 19618–19625.
37 L.-W. Wang, *Phys. Rev. Lett.*, 2012, **108**, 085703.
38 T. J. Trentler, K. M. Hickman, S. C. Goel, A. M. Viano, P. C. Gibbons and W. E. Buhro, *Science*, 1995, **270**, 1791–1794.
39 Q. Gao, V. G. Dubrovskii, P. Caroff, J. Wong-Leung, L. Li, Y. Guo, L. Fu, H. H. Tan and C. Jagadish, *Nano Lett.*, 2016, **16**, 4361–4367.
40 E. Oksenberg, E. Sanders, R. Popovitz-Biro, L. Houben and E. Joselevich, *Nano Lett.*, 2018, **18**, 424–433.

